ARMA 16-678

UAV-Based 3-D Characterization of Rock Masses and Rock Slides in Nepal

Greenwood, W., Zekkos, D., Lynch J., and Bateman, J.
University of Michigan, Department of Civil and Environmental Engineering, Ann Arbor, MI, USA
Clark, M. K.
University of Michigan, Department of Earth and Environmental Science, Ann Arbor, MI, USA
Chamlagain, D.
Tribhuvan University, Tri-Chandra Multiple Campus, Department of Geology, Kathmandu, Nepal

ABSTRACT: Unmanned aerial vehicles (UAV) have the potential to become powerful site reconnaissance and data collection tools for in geoengineering. UAVs are expected to become particularly useful in geomechanics applications such as rock mass characterization, landslide imaging, and failure analysis, as part of post-disaster reconnaissance, or conventional engineering practice. A low-cost quadrotor UAV has been used as a data acquisition platform for optical imagery at a number of sites affected by the 2015 Gorkha earthquake in Nepal. The UAV collected images of landslides that would normally be very difficult, or expensive to access. Two example landslides are presented in this contribution. Structure-from-motion photogrammetry was used to generate 3-D point clouds and meshes for each site. These models were geometrically scaled using field survey measurements and used as the primary component of a landslide rock characterization scheme. 3-D models were also used to define landslide post-failure geometry. Models were used to delineate the orientation of 3-D features in the rock structure such as fractures, bedding, foliation, and stratigraphy. Multiple failure modes, including wedge failures, were also identified from 3-D models. The results of this study demonstrate the capabilities of UAVs as a tool for characterization and data collection at rock sites.

1. INTRODUCTION

The popularity of unmanned aerial vehicles (UAV), or drones, has increased in recent years. UAVs have been used to collect optical imagery related to many engineering applications (Lin et al., 2015; Gillins et al., 2016; among others). Most commonly, the collected imagery is only used for qualitative assessments. Recent efforts have been made to introduce more quantitative assessments (Ellenberg et al., 2014; Hugenholtz et al., 2015), however, more advancements are needed to fully exploit the collected data. The increasing prevalence of UAVs along with rapidly advancing technology, presents a tremendous opportunity for UAV platforms to become powerful data collection tools in geoengineering. New technologies coupled with established imaging methods allow for low-cost UAV platforms to be useful for many geomechanics applications.

As part of this study, a low-cost quadrotor UAV was used to collect optical images at two sites affected by the M_w 7.8 2015 Gorkha earthquake in Nepal. These two sites are presented as examples of using a UAV platform to investigate co-seismic landslides and characterize rock mass structure. Structure-from-motion (SFM) photogrammetry was used to generate scaled, 3-D models of the landslides using the UAV-collected imagery. The images and scaled models were then used for a quantitative assessment of the rock mass at each site that included an assessment of spacing and orientation of discontinuities, exposed rock mass structure and stratigraphy characterization, as well as slope geometry. The value of using 3-D point clouds to perform these characterizations is also discussed.

2. 2015 GORKHA EARTHQUAKE

On April 25, 2015 the Gorkha earthquake (M_w = 7.8) caused widespread damage across Nepal. The series of aftershocks was headlined by the May 12, 2015 event (M_w = 7.3). Epicenters of the April 25, 2015 earthquake and other major events are shown in Figure 1. The main earthquake epicenter was located about 80 km northwest of Kathmandu and resulted in a 140 km rupture segment along the Main Himalayan Thrust (Galetzka et al., 2015). Previous major seismic events in this region are discussed by Hayes et a., 2015. This event resulted in

nearly 9000 fatalities and destroyed over 500,000 homes resulting in millions of displaced people (NSET, 2015). There have been several post-earthquake reconnaissance investigations into the damage caused by the earthquake (Chiaro et al., 2015; Collins and Jibson et al., 2015; Hashash et al., 2015).

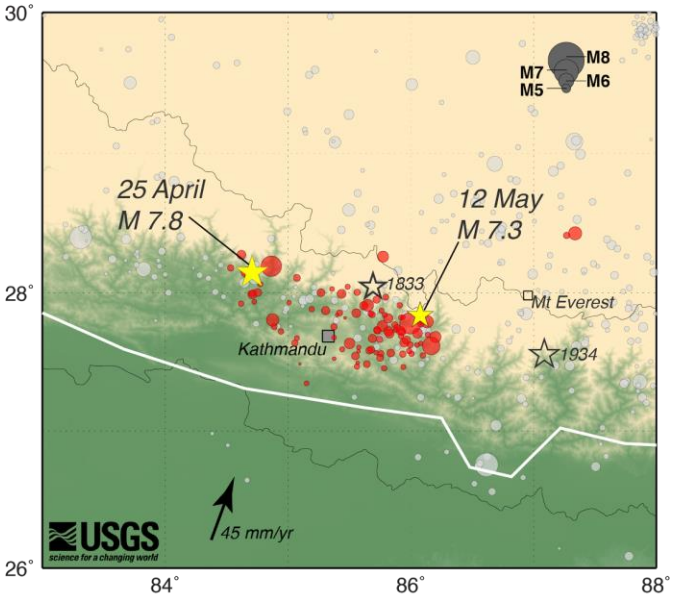

Fig. 1. Mainshock and distributed aftershocks of the 2015 Gorkha earthquake sequence (from Robertson and Koontz, 2015).

The earthquake caused tens of thousands of landslides throughout the affected region (Clark et al., 2015; Collins and Jibson et al., 2015; Gallen et al., 2016; Kargel et al., 2015). Landsliding was magnified by the steep mountainous terrain of Nepal and has had a profound impact on the region. Landslides varied in size and resulted in destruction of infrastructure, loss of life and, in some cases, destruction of entire villages. A wide variety of landslide types has been attributed to the Himalaya in other studies (Timilsina et al., 2014). The majority of landslides during the Gorkha earthquake occurred within the Greater Himalayan and Lesser Himalayan tectonostratigraphic units. The Greater Himalayan units are characterized by medium to high-grade schist and gneisses granitic plutons, and the Lesser Himalayan units are characterized by low-grade metasedimentary rocks (e.g. Schelling, 1992; Le Fort, 1986; Gansser, 1964).

3. UAV PLATFORM

The industry of small unmanned aerial vehicles has grown tremendously in recent years. During the first 30 days of the United States Federal Aviation Administration's (FAA) small unmanned aerial systems registration program, which began in December 2015, the FAA reported the registration of nearly 300,000 owners (FAA, 2016). The high demand for small UAVs has driven rapid technology advancements. Small UAVs have become much more affordable and are beginning to be used in many public and private sector industries including:

- Law Enforcement (Straub, 2014)
- Precision Agriculture (Aasen et al., 2015)
- Archaeology (Agapiou and Lysandrou, 2015)
- Infrastructure and Structural Assessment (Li et al., 2013)
- Geotechnical Site Characterization (Zekkos et al., 2014)

The most commonly used small UAVs, for both scientific and recreational uses, are constructed to carry and operate an optical camera. As previously mentioned, with rapid technology advancements, small UAVs have become more affordable and flexible for different applications. However, the cost of a camera-equipped UAV can vary significantly due to a variety of factors including:

- Vehicle type (multirotor versus fixed-wing)
- Maximum payload
- Maximum flight time
- Compatible camera and sensors
- Software capabilities (autopilot, analysis software)
- Integrated components (flight controller, GPS)

The camera-equipped UAV used as part of this study was the Phantom 3 Professional (P3P) from DJI. The P3P operates with an integrated optical camera coupled to the UAV with a triaxial gimbal. The camera is capable of collecting still photos and high-definition video. Some details of the P3P UAV platform and the integrated camera are outlined in Table 1. The P3P and related platforms have been used in other recent studies including those related closely to civil engineering applications (Gillins et al., 2016). The P3P UAV platform is shown in flight in Figure 2.

Table 1. DJI Phantom 3 Professional UAV and camera specifications.

Phantom 3 Professional UAV	
Aircraft Weight	1.28 kg
Diameter	59 cm
Maximum Velocity	16 m/s
Maximum Flight Time	23 minutes
Integrated P3P Camera	
Sensor Size	1/2.3 in.
Maximum Aperture	f/2.8
FOV	94°
Maximum Photo Resolution	4000 x 3000 Pixels
Maximum Video Resolution	4096 x 2160 Pixels

Recently, low-cost UAVs used have been used in landslide investigations. A low cost UAV was used to investigate the Super-Sauze landslide near Grenoble, France by Niethammer et al., 2012. Murphy et al., 2015 deployed three commercially available small UAVs to visually characterize the 2014 Oso landslide in Washington.

Fig. 2. DJI Phantom 3 Professional platform used in field reconnaissance.

4. IMAGING METHODS

4.1. Imaging in Rock Mechanics

In general, optical imagery and other types of remote sensing have been used in rockslide investigations and analyses. 3-D imaging and remote sensing methods are particularly useful (Brückl et al., 2006; Collins and Stock, 2012). Brückl et al., 2006 used photogrammetry to define geometry for kinematic derivations of a deep-seated landslide. Collins and Stock, 2012 used terrestrial laser scanning to characterize rockfall hazards along cliffs. Recently, new processing methods for 3-D geometric data are being investigated with some focus on automated, or semi-automated techniques (Vöge et al., 2013; Gigli and Casagli, 2011). Sturzenegger and Stead, 2009 used terrestrial photogrammetry and laser scanning to investigate discontinuities in mountain rock-slopes and landslides. Riquelme et al., 2015 used 3-D point clouds to analyze discontinuity spacing in rock structures.

4.2. Structure-From-Motion Photogrammetry

SFM photogrammetry was used to develop 3-D point cloud models of landslide sites. Image processing and 3-D point cloud production was performed using a commercially available software (Pix4D, 2016). SFM has been an established imaging method for many years. It has been used effectively in many geological and geotechnical engineering applications (Romo and Keaton, 2013; Westoby et al., 2012; Cleveland and Wartman, 2006; Oka 1998). Hryciw et al. 2014 provides an overview of how imaging methods have been used in geotechnical and engineering geology. A description of applied SFM photogrammetry is provided in Westoby et al., 2012.

Data is collected in the form of optical imagery. Collection could be a series of still photos or frames extracted from a video. In order for 3-D information to be interpreted from 2-D images, sufficient overlap between successive images is required. Typically, at least 60% overlap between images is recommended for 3-D model generation. The technique requires a mobile camera and a method to physically measure objects in order to properly scale the 3-D model. Traditionally, data is collected by a person on the ground who manually relocates the camera. Data processing for this imaging method is, in general, computationally intensive. Modern software, algorithms, and computer technology have greatly alleviated this allowing for larger, more detailed, 3-D models to be generated more quickly.

5. FIELD INVESTIGATION

Data was collected using the UAV in the form of optical imagery, through still photos or videos. Traditionally, still photos have primarily been used for photogrammetric data collection. This is because photos, in general, have significantly greater resolutions compared to video frames. This means that additional effort must be made to ensure sufficient overlap between images. With the advent of HD video and, more recently, 4K video, the advantage of using still photos over video frames has become less significant. In fact, video allows for a stream of images to be collected while greatly reducing the concern for acquiring the necessary overlap between images. However, processing of video frames at high frequencies can become computationally intensive. For these reasons, both video and photos were used to collect images of each investigated site depending on the complexity of features and possible flight limitations.

The UAV was manually flown from the ground to reposition the camera for data collection. Ground control point (GCP) targets, generally about 3-8 in total, were placed at the sites where accessible. The distances between these GCP targets were measured manually, using triangulation, using a measuring tape as well as a handheld GPS unit. The GCP targets are easily detected in imagery and, usually, in 3-D point clouds. An example of a deployed GCP target is shown in Figure 3. A tripod-mounted laser was also used to measure the distance between points-of-interest on the landslides.

During 3-D model development, a portion of GCP targets and/or points of interest were used in image processing to correctly scale the 3-D model. The remaining points were used to acquire a verification of model scaling and a spatially-distributed estimate of the model error.

Frames were extracted from videos at an adequate rate for sufficient overlap. The rate of frame extraction varies depending on the velocity of the UAV and the distance to the object of interest. Images were then corrected for lens distortion. Photogrammetry software was then used with the final image sets to generate 3-D point clouds of each site. Image data was collected for a total of 15 landslides. Two example landslides are shown in this contribution.

Fig. 3. Example of deployed GCP target.

6. LANDSLIDE SITE 1

6.1. Overview

The first landslide site (Landslide 1) was located about 30 km northeast of Kathmandu, near Melamchi. At this site a roughly 75 m high rock-slope failed. The slope is, on average, angled at about 70° from the horizontal. However, the top 5 m of the slope is angled at about 50°. The rockslide is indicative of a failure of a broken-up rock mass that is mechanically characterized as Hoek and Brown strength material (Hoek and Brown, 1980). An overview of the rockslide is shown, as a point cloud, in Figure 4. The 3-D point cloud was generated from 257 images of the site. The debris cone outlined in Figure 4 is sloping at about 35°. The landslide scarp exposes the rock mass structure over an area that is approximately 40 m high and 45 m wide. The distribution of GCP at this site is shown in Figure 5. The targets are placed in accessible locations on the landslide debris. An annotated cross-section through the point cloud is shown in Figure 6. The 3-D point cloud has a mean resolution of 6 cm/pixel. Images collected perpendicular to the landslide scarp were collected at two distances, roughly 30 m and 70 m. The UAV was flown as close as 15 m above the debris cone.

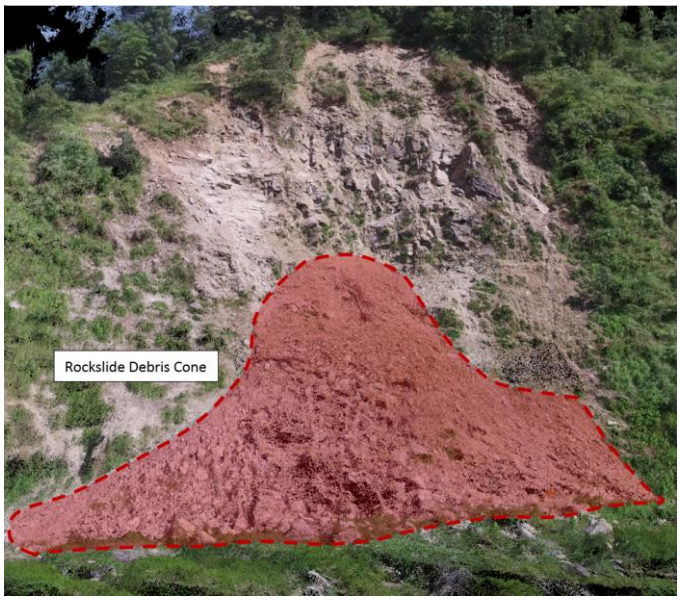

Fig. 4. Overview of Landslide 1, near Melamchi (3-D point cloud).

Fig. 5. GCP locations on Landslide 1 debris.

6.2. Interpretations

Generalized stratigraphy can be interpreted from the visual observations of the collected imagery and the 3-D point cloud. These interpretations were investigated in the 3-D point cloud in order to characterize the discontinuities in the rock mass and overall rock structure. As shown in Figure 7, the surface layer at the top of the slope is about 5 m thick and contains predominantly soil and extremely weathered rock. The remainder of the exposed rock can be separated into two

additional sections. A shallower layer, located between about 5 m and 15 m from the top of slope. This layer is more weathered rock with dominant horizontal foliation, and classifies as disintegrated rock per Marinos et al., 2005. The Geological Strength Index (GSI) is a critical parameter for the geomechanical characterization of the rock mass structure and is a function of the rock structure and the weathering condition of discontinuities. According to visual observations, the GSI for this layer is estimated to be on the order of 25-45. Horizontal fractures are spaced at 0.4 – 0.8 m throughout the layer. The next layer is located between 15 m from the top of the slope to the base. This layer is less broken-up rock with perpendicular vertical/horizontal fracturing aligned with the slope face, and classifies as blocky per Marinos et al., 2005. The GSI for this layer is estimated to be on the order of 45-65. The spacing of horizontal fractures is 2 – 3 m and the spacing of vertical fractures is 0.3 – 0.9 m. A delineation of the landslide layers in the point cloud is shown in Figure 8. It should be noted that, beyond about 40 m from the top of slope, the rock structure is hidden by the slide debris at the bottom of the slope. A small portion of rock was exposed near the top of the debris cone and indicated dominant horizontal foliation. However, the persistence of this structure cannot be confirmed without excavation or extensive investigation of the slope.

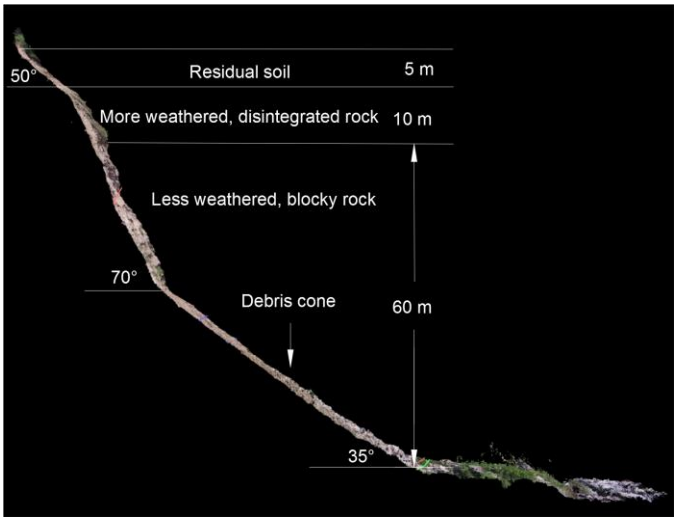

Fig. 6. Cross-section of Landslide 1 point cloud.

The final rendered model of the rock-slope had a mean resolution of 6 cm/pixel. This means that in general, features in the rock structure smaller than 6 cm cannot possibly be observed. Areas of higher and lower resolution do exist, and are dependent on the flight parameters. Because of this point cloud density, not all features of the rock mass that are visible in 2-D images can be detected in the 3-D point cloud. These include foliation and fractures with small spacing relative to the point cloud resolution. It should be noted that for measuring many of these discontinuities, color, rather than 3-D point position must be relied upon. This means that in most cases discontinuities could only be detected based on observed changes in color. This implies some reliance on the accompanying 2-D images for delineating discontinuities and rock features in the point cloud. In order to detect discontinuities based in the position of 3-D points, a higher density, higher resolution point cloud would be required as well as a measure of changes in surface roughness. An automated operation can be used to determine surface roughness in the point cloud.

Fig. 7. 2D View of the back-scarp of Landslide 1 where the top two layers of the weathering profile can be seen.

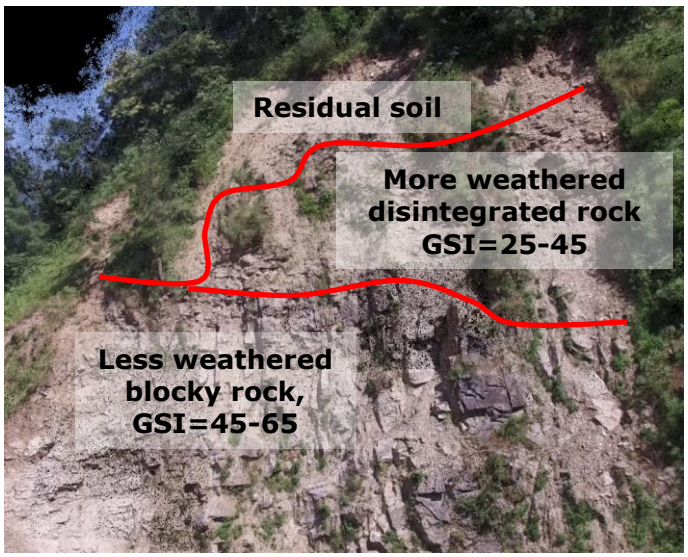

Fig. 8. 3D point cloud of the back-scarp of Landslide 1 with annotated layers and Geologic Strength Index (GSI) parameters per Marinos et al., 2005.

7. LANDSLIDE SITE 2

7.1. Overview

The second landslide site (Landslide 2) investigated in this study was located about 28 km east of Kathmandu. The failure occurred on a roughly 150 m high slope angled at about 65° from horizontal. An overview of the rockslide is shown, as a point cloud, in Figure 9. Unlike Landslide 1, Landslide 2 appears to have exhibited a combination of modes of failure. The rockslide is characterized by a shallow failure of a broken-up rock mass up-slope of a structurally-controlled, wedge type failure. The distribution of GCP and laser points is shown in Figure 10. GCP were placed on the landslide debris field and along the road adjacent to the base of the landslide. Laser points are located both in the debris field and on the landslide scarp. The UAV was flown as close as 40 m and as far as 80 m from the landslide scarp near the top of the slope. At the structurally-controlled failure, the UAV's camera was positioned 10-15 m away. This allowed for improved detail in the images of the rock structure at this critical location.

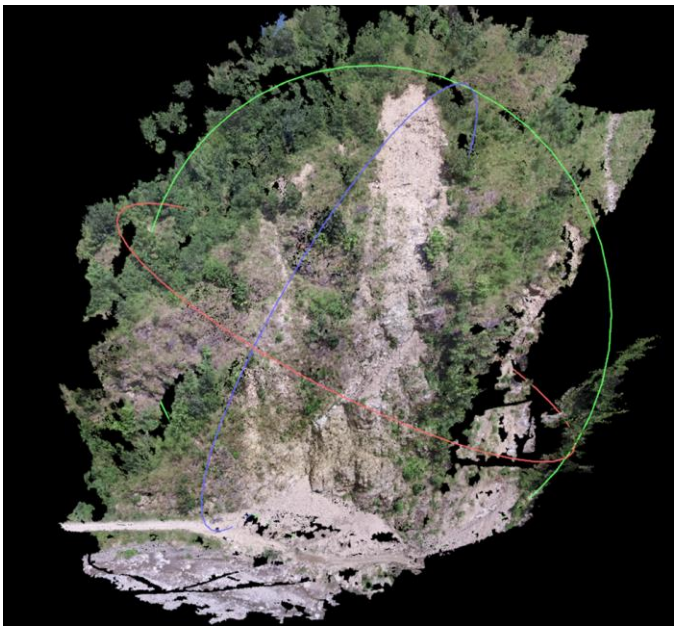

Fig. 9. Overview of Landslide 2, east of Kathmandu.

7.2. Interpretations

As with Landslide 1, the spacing and orientation of discontinuities was observed in the 2-D images and subsequently measured in the scaled 3-D point cloud. A layer of soil and extremely weathered rock is located in the top 12 m of the slope. In general, the visible rock structure is dominated by foliation with a strike of 255°, dipping at 20° to the northwest. A weathering profile is apparent with a decreasing degree of weathering downslope. The structurally-controlled, wedge failure is located at approximately one third of the slope height. The failure is shown in the 3-D point cloud in Figure 11. A large block of the material was observed on the landslide debris along the road, probably originating from the failed wedge.

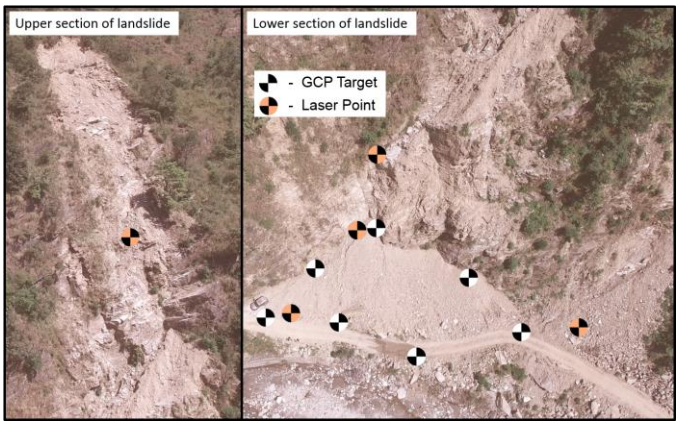

Fig. 10. Distribution of GCP and laser points on Landslide 2.

Fig. 11. Possible structurally-controlled failure in Landslide 2.

The rock, at this point, has few vertical fractures and is governed by foliation. Similar to Landslide 1, there is evidence in the 2-D imagery of foliation in the rock. However, in this case, the foliation is also visible in some sections of the 3-D model. This is due to the improved model resolution of Landslide 2 compared to Landslide 1. The mean resolution of this model is 1.2 cm/pixel, compared to 6 cm/pixel previously. In the sections of the model with the greatest resolution, small features and discontinuities are visible, such as the foliation. The improved resolution in this model is primarily due to the flight path taken by the UAV. The camera was positioned significantly closer to the

landslide directly leading to improved resolution of the visible rock structure.

8. CONCLUSIONS

A total of 15 landslides were mapped in a field expedition to characterize the landslide patterns caused by the 2015 Gorkha earthquake in Nepal using a small, low-cost UAV-mounted camera. Two example landslides are presented in this contribution. Optical images of the landslides and the rock structure were collected and used as part of a structure-from-motion photogrammetry scheme to generate 3-D point clouds of each landslide. The resultant 3-D point clouds were used to demonstrate their usefulness in 3-D rock mass characterization. Limitations of using 3-D point clouds for interpreting rock structure are also discussed. Based on the observations made in this study, the following conclusions can be made about the advantages of using UAV-generated 3-D point clouds in rock characterization:

- At most scales, the 2-D input imagery and the 3-D result provide similar qualitative information.
- With an appropriate, field-measured scale any visible object can be measured for size and orientation
- The UAV can be used to collect imagery much more efficiently than terrestrial photogrammetry, especially for high, steep and largely inaccessible slopes.
- The UAV can be used to minimize occlusion and maximize resolution at critical locations.
- Adjustments to the UAV path should be made based on visual observations during flight to acquire the necessary image resolution for certain rock features.

9. ACKNOWLEDGEMENTS

This research was supported by the National Science Foundation (NSF), Division of Civil and Mechanical Systems under Grant No. CMMI-1362975 and NSF, Division of Earth Sciences RAPID Geomorphology and Land Use Dynamics Collaborative Research Grant No. 1546631. ConeTec Investigations Ltd. and the ConeTec Education Foundation (ConeTec) are also acknowledged for their support to the Geotechnical Engineering Laboratories at the University of Michigan. Any opinions, findings, conclusions and recommendations expressed in this paper are those of the authors and do not necessarily reflect the views of the NSF, or ConeTec.

REFERENCES

1. Aasen, H., A. Burkart, A. Bolten, and G. Bareth. 2015. Generating 3D hyperspectral information with lightweight UAV snapshot cameras for vegetation monitoring: from camera calibration to quality assurance. *ISPRS J. of Photogrammetry and Remote Sensing*. 108: 245-259.

2. Agapiou, A., and V. Lysandrou. 2015. Remote sensing archaeology: tracking and mapping evolution in European scientific literature from 1999 to 2015. *J. of Archaeological Sci*. 4: 192-200.

3. Brückl, E., F. K. Brunner, and K. Kraus. 2006. Kinematics of a deep-seated landslide derived from photogrammetric, GPS and geophysical data. *Engineering Geology*. 88: 149-159.

4. Chiaro, G., T. Kiyato, R. M. Pokhrel, K. Goda, T. Katagiri, and K. Sharma. 2015. Reconnaissance report on geotechnical and structural damage caused by the 2015 Gorkha earthquake, Nepal. *Soils and Foundations*. 55(5): 1030-1043.

5. Clark, M. K., S. Gallen, A. J. West, D. Chamlagain, K. Roback, K. Lowe, N. Niemi, W. Greenwood, J. Bateman, D. Zekkos. 2015. Coseismic landslides associated with the 2015 Gorkha earthquake sequence in Nepal. (Invited) *Eos Trans.*, Fall Meet. Suppl., Abstract Session S42C-02.

6. Collins, B. D., and R. W. Jibson. 2015. Assessment of existing and potential landslide hazards resulting from the April 25, 2015 Gorkha, Nepal earthquake sequence. *U.S. Dept. of the Interior, U.S. Geological Survey*, Open-File Report 2015-1142, August 2015.

7. Collins, B. D., and G. M. Stock. 2012. Lidar-based rock-fall characterization of cliffs. *GeoCongress 2012*, Oakland, CA, 25-29 March 2012, eds. R. D. Hryciw et al. 3021-3030.

8. Cleveland, L.J., and J. Wartman. 2006. Principles and applications of digital photogrammetry for geotechnical engineering. Site and Geomaterial Characterization, Shanghai, China, 6-8 June 2006, eds. A. J. Puppala et al.128-135.

9. Ellenberg, A., L. Branco, A. Krick, I. Bartoli, and A. Kontsos. 2014. Use of Unmanned aerial vehicle for quantitative infrastructure assessment. *J. Infrastructure Systems*. 21(3): 04014054.

10. FAA. 2016. FAA registered nearly 300,000 unmanned aircraft owners. 22 January 2016, <http://www.faa.gov/news/press_releases/news_story.cfm?newsId=19914>.

11. Galetzka, J., D. Melgar, J. F. Genrich, J. Geng, S. Owen, E. O. Lindsey, X. Xu, Y. Bock, J.-P. Avouac, L. B. Adhikari, B. N. Upreti, B. Pratt-Sitaula, T. N. Bhattarai, B. P. Sitaula, A. Moore, K. W. Hudnut, W. Szeliga, J. Normandeau, M. Fend, M. Flouzat, L. Bollinger, P. Shrestha, B. Koirala, U. Gautam, M. Bhatterai, R. Gupta, T. Kandel, C. Timsina, S. N. Sapkota, S. Rajaure, and N. Maharjan. 2015. Slip pulse and resonance of the Kathmandu basin during the 2015 Gorkha earthquake, Nepal. *Science*. 349: 1091-1095.

12. Gallen, S., M. Clark, J. Godt, K. Roback, and N. Niemi. (In Review). Application of a rapid response earthquake-triggered landslide model to the 25 April 2015 M_w 7.8 Gorkha earthquake, Nepal. *Tectonophysics*.

13. Gansser, A. 1964. Geology of the Himalayas. London: Wiley Interscience.

14. Gigli, G., and N. Casagli. 2011. Semi-automatic extraction of rock mass structural data from high resolution lidar point clouds. *J. of Rock Mechanics & Mining Sciences*. 48: 187-198.

15. Gillins, M. N., D. T. Gillins, and C. Parrish. 2016. Cost-effective bridge safety inspections using unmanned aerial systems (UAS). Geotechnical and Structural Engineering Congress 2016, 14-17 February 2016, Phoenix, AZ, eds. Y. Chandran et al. 1931-1940.

16. Hashash, Y. M. A., B. Tiwari, R. E. S. Moss, D. Asimaki, K. B. Clahan, D. S. Kieffer, D. S. Dreger, A. Macdonald, C. M. Madugo, H. B. Mason, M. Pehlivan, D. Rayamajhi, I. Acharya, and B. Adhikari. 2015. Geotechnical field reconnaissance: Gorkha (Nepal) earthquake of April 25 2015 and related shaking sequence. GEER Association Report No. GEER-040. 7 August 2015.

17. Hayes, G. P., R. W. Briggs, W. D. Barnhart, W. L. Yeck, D. E. McNamara, D. J. Weld, J. L. Nealy, H. M. Benz, R. D. Gold, K. S. Jaiswal, and K. Marano. 2015. Rapid characterization of the 2015 M_w 7.8 Gorkha, Nepal earthquake sequence and its seismotectonic context. *Seismological Research Letters*. 86(6): 1557-1567.

18. Hoek E., and E. T. Brown. 1980 Empirical strength criterion for rock masses. *J. Geotech. Engng Div.*, ASCE 106(GT9), 1013-1035.

19. Hryciw, R. D., J. Zheng, H.-S. Ohm, and J. Li. 2014. Innovations in optical geo-characterization. GeoCongress 2014 Keynote Lectures, Atlanta, GA, 23-26 February 2014, eds. A. J. Puppala et al. 97-116.

20. Hugenholtz, C. H., J. Walker, O. Brown, and S. Myshak. 2014. Earthwork volumetrics with an unmanned aerial vehicle and softcopy photogrammetry. *J. of Surveying Engineering*. 141(1): 06014003.

21. Kargel, J. S., G. J. Leonard, D. H. Shugur, U. K. Haritashya, A. Beyington, E. J. Fielding, K. Fujita, M. Geertsema, E. S. Miles, J. Steiner, E. Anderson, S. Bajracharya, G. W. Bawden, D. F. Breashears, A. Byers, B. Collins, M. R. Dhital, A. Donnellan, T. L. Evans, M. L. Geai, M. T. Glasscoe, D. Green, D. R. Gurung, R. Heijenk, A. Hilborn, K. Hudnut, C. Huyck, W. W. Immerzeel, J. Liming, R. Jibson, A. Kääb, N.R. Khanal, D. Kirschbaum, P. D. A. Kraaijenbrink, D. Lamsal, L. Shiyin, L. Mingyang, D. McKinney, N. K. Nahirnick, N. Zhoutong, S. Ojha, J. Olsenholler, T. H. Painter, M. Pleasants, K. C. Pratima, Q. I. Yuan, B. H. Raup, D. Regmi, D. R. Rounce, A. Sakai, S. Donghui, J. M. Shea, A. B. Shrestha, A. Shukla, D. Stumm, M. van der Kooij, K. Voss, W. Xin, B. Weihs, D. Wolfe, W. Lizong, Y. Xiaojun, M. R. Yoder, and N. Young. 2016. Geomorphic and geologic controls of geohazards induced by Nepal's 2015 Gorkha earthquake. *Science*. 351: DOI: 10.1126/science.aac8353.

22. Le Fort, P. 1986. Metamorphism and magnetism during the Himalayan collision. *Geological Society, London, Special Publications*. 19.1: 159-172.

23. Li. H., S. Dong, S. El-Tawil, and V. R. Kamat. 2013. Relative displacement sensing techniques for post-event structural damage assessment: review. *J. of Structural Engineering*. 139(9): 1421-1434.

24. Lin, J. J., K, K., Han, and M. Golparvar-Fard. 2015. A framework for model-driven acquisition and analytics of visual data using UAVs for automated construction progress monitoring. Computing in Civil Engineering 2015, Austin, TX, 21-23 June 2015, eds. W. J. O'Brien et al. 156-164.

25. Marinos V., P. Marinos, E. Hoek. 2005. The geological strength index: applications and limitations. Bull. Eng. Geol. Environ., 64, 55-65

26. Murphy, R. R., B. A. Duncan, T. Collins, J. Kendricks, P. Lohman, T. Palmer, and F. Sanborn. 2015. Use of a small unmanned aerial system for the SR-530 mudslide incident near Oso, Washington. *J. of Field Robotics*. DOI: 10.1002/rob.21586.

27. Moss, R. E. S., E. M. Thompson, D. S. Kieffer, B. Tiwari, Y. M. A. Hashash, I. Acharya, B. R. Adhikari, D. Asimaki, K. B. Clahan, B. D. Collins, S. Dahal, R. W. Jibson, D. Khadka, A. Macdonald, C. L M. Madugo, H. B. Mason, M. Pehlivan, D. Rayamajhi, and S. Uprety. 2015. Geotechnical effects of the 2015 magnitude 7.8 Gorkha, Nepal earthquake and aftershocks. *Seismological Research Letters*. 86(6): 1514-1523.

28. Niethammer, U., M. R. James, S. Rothmund, J. Travelletti, and M. Joswig. 2012. UAV-based remote sensing of the Super-Sauze landslide: evaluation and results. *Engineering Geology*. 128: 2-11.

29. NSET. 2015. National Society for Earthquake Technology – Nepal. 25 May 2015, < http://www.nset.org.np/eq2015/>.

30. Oka, N. 1998. Application of photogrammetry to the field observation of failed slopes. *Engineering Geology*. 50: 85-100.

31. Pix4D. 2016. Advanced photogrammetry software to create orthomosaics, point clouds, and models. <http://www.pix4d.com/>.

32. Riquelme, A. J., A. Abellán, and R. Tomás. 2015. Discontinuity spacing analysis in rock masses using 3D point clouds. *Engineering Geology*. 195: 185-195.

33. Robertson, J., and H. Koontz. 2015. Magnitude 7.8 earthquake in Nepal and Aftershocks. 12 May 2015, <http://www.usgs.gov/blogs/features/usgs_top_story/magnitude-7-8-earthquake-in-nepal/>.

34. Romo P. E., and J. R. Keaton. 2013. Reconnaissance documentation of geologic structure using close-range terrestrial photogrammetry. GeoCongress 2013, San Diego, CA, 3-7 March 2013, eds. C. Meehan et al. 1578-1586.

35. Schelling, D. 1992. The tectonostratigraphy and structure of the eastern Nepal Himalaya. *Tectonics*. 11(5): 925-943.

36. Straub, J. 2014. Unmanned aerial sustems: consideration of the use of force for law enforcement applications. *Technology in Society*. 39: 100-109.

37. Sturzenegger, M., and D. Stead. 2009. Quantifying discontinuity orientation and persistence on high mountain rock slopes and large landslides using terrestrial remote sensing techniques. *Natural Hazards and Earth System Sciences*. 9: 267-287.

38. Vöge, M., M. J. Lato, and M. S. Diederichs. 2013. Automated rockmass discontinuity mapping from 3-dimensional surface data. *Engineering Geology*. 164: 155-162.

39. Westoby, M. J., J. Brasington, N. F. Glaser, M. J. Hambrey, and J. M. Reynolds. 2012. 'Structure-from-motion' photogrammetry: a low-cost tool for geoscience applications. *J. of Geomorphology*. 179: 300-314.

40. Zekkos, D., J. Lynch, A. Sahadewa, M. Hirose, and D. Ellis. 2014. Proof-of-concept shear wave velocity measurement using an unmanned autonomous aerial vehicle. GeoCongress 2014, Atlanta, GA, 23-26 February 2014, eds. A. J. Puppala et al. 953-962.

41. Zhou, Z., J. Gong, and M. Guo. 2015. Image-based 3D reconstruction for posthurricane residential building damage assessment. *J. of Computing in Civil Engineering*. 04015015.